Inertial torsion noise in matter-wave interferometers for gravity experiments

Meng-Zhi Wu,[1,*] Marko Toroš,[2] Sougato Bose,[3] and Anupam Mazumdar[1,†]

[1]*Van Swinderen Institute for Particle Physics and Gravity, University of Groningen, 9747 AG Groningen, The Netherlands*

[2]*Faculty of Mathematics and Physics, University of Ljubljana, Jadranska 19, SI-1000 Ljubljana, Slovenia*

[3]*Department of Physics and Astronomy, University College London, Gower Street, WC1E 6BT London, United Kingdom*

(Received 6 May 2024; accepted 22 January 2025; published 3 March 2025)

Matter-wave interferometry is susceptible to noninertial noise sources, which can induce dephasing and a resulting loss of interferometric visibility. Here, we focus on inertial torsion noise (ITN), which arises from the rotational motion of the experimental apparatus suspended by a thin wire and subject to random external torques. We provide analytical expressions for the ITN noise starting from generalized Langevin equations describing the experimental box, which can then be used together with the transfer function to obtain the dephasing factor. We verify the theoretical modeling and the validity of the approximations using Monte Carlo simulations, obtaining good agreement between theory and numerics. As an application, we estimate the size of the effects for the next generation of interferometry experiments with femtogram particles, which could be used as the building block for entanglement-based tests of the quantum nature of gravity. We find that the ambient gas is a weak source of ITN, posing mild restrictions on the ambient pressure and temperature. We discuss the general ITN constraints by assuming a Langevin equation parametrized by three phenomenological parameters.

DOI: 10.1103/PhysRevD.111.064004

I. INTRODUCTION

Matter-wave interferometry has many salient applications for gravitational physics with devices spanning gravimeters [1], gradiometers [2,3], accelerometers [4], and gyroscopes [5]. They can also be used for fundamental physics, such as testing the equivalence principle [6–8] and the quantum gravity induced entangled of masses (QGEM) to test the quantum nature of gravity in a lab [9,10]; see also [11–14]. The paper [14] provided the protocol to test the spin-2 nature of the graviton in an analogue of the light-bending experiment; see also [13]. One can also probe the nature of massive gravitons [15] and nonlocal gravitational interactions [16] motivated by string theory. Furthermore, some groups even considered building gravitational-wave observatories based on matter-wave interferometry, such as the matter-wave laser interferometer gravitation antenna [17,18], the matter-wave atomic gradiometer interferometric sensor [19,20], and the mesoscopic interference for metric and curvature scheme [21].

Future matter-wave interferometry aims to exploit the regime of large masses, large superposition sizes, and long coherence times, allowing for probes of exquisitely small experimental signals. For example, the QGEM experiment would ideally require a test mass of $\sim 10^{-15}$ kg, a superposition size of ~ 100 μm, and a coherence time of ~ 1 s [8,9,22–24]. One of the most promising setups towards this kind of experiments is the adaptation of the Stern-Gerlach interferometer (SGI) to nanoparticles [25]. SGIs based on atom chips [26] have already achieved a superposition size and coherence time of 3.93 μm and 21.45 ms for the half-loop configuration, respectively [26], and 0.38 μm and 7 ms for the full-loop configuration, respectively [27]. The next generation of SGIs is currently under theoretical and numerical investigation [28–32].

An essential challenge of matter-wave interferometry is to tame the numerous noise sources, which can cause random phase fluctuations, resulting in dephasing and the loss of interferometric visibility. Vibrations of the experimental apparatus can result in residual acceleration noise [33,34], external sources of gravity can induce gradient noise [18,20,34,35], and charged or dipolar environmental particles can induce several electromagnetic channels of dephasing [36,37], besides gravitational decoherence [38] of the QGEM.

This paper studies the dephasing caused by the residual rotational or inertial torsion noise (ITN) for an asymmetric nanoparticle matter-wave interferometer, which is sensitive to gravity gradients [21,34,35]. ITN arises naturally in any

*Contact author: mengzhi.wu@rug.nl

†Contact author: anupam.mazumdar@rug.nl

setup whenever the experimental apparatus is subject to random torques, placing it in noninertial rotational motion. As we will see, ITN can induce relative random phases in an interferometric experiment, resulting in a loss of interferometric contrast. Here, we are primarily interested in understanding ITN and focus on a simple single-stage suspension forming a torsion pendulum, i.e., matter-wave interferometry performed inside a hanging box. Analogous configurations of the experimental apparatus were investigated previously in gravitational-wave observatories like LIGO [39] and Virgo [40]. More advanced setups could employ additional structures like the inverted pendulum [41] and the Roberts linkage [42].

In Sec. II, we first introduce the concept of ITN, illustrating it for matter-wave interferometry that can be modeled using qubits. In Sec. III, we generalize the analysis using linear response theory, providing the transfer function and its relation to the dephasing factor. In Sec. IV, we investigate ITN caused by ambient gas collisions on the experimental box starting from a generalized classical Langevin equation. We compute the power spectrum density (PSD) of the ITN using the convolution theorem and verify the validity of the approximations using Monte Carlo simulations. In Sec. V, we obtain the resulting constraints on the ambient pressure and temperature and general constraints on ITN by parametrizing a generic Langevin equation modeling the experimental box with three phenomenological parameters in the dynamical equation of the experimental box. In Sec. VI, we conclude with a summary of the obtained results. In Appendix A, we construct the ITN Lagrangian starting from Fermi normal coordinates and transforming to a rotating reference frame. In Appendix B, we provide for completeness the complete derivation of the ITN PSD using complex analysis. In Appendix C, we analyze the ITN caused by ambient thermal gas collisions.

II. CONCEPT OF INERTIAL TORSION NOISE AND DEPHASING

Suppose the interferometer is set up in a suspended experimental apparatus, as shown in Fig. 1(a). A natural reference frame is the comoving frame of the experimental apparatus. For instance, consider a Stern-Gerlach interferometer controlled by a static magnetic field $\mathbf{B}(x, y, z)$, which holds for the comoving frame of the experimental apparatus. If the SGI is studied under another reference frame that moves relative to the comoving reference, then the Lorentzian transformation of the magnetic field $\mathbf{B}(t)$ has to be taken into account, and even the induced electric field also needs to be studied. The comoving reference frame of the experimental apparatus is thus preferred as it simplifies the analysis.

However, the experimental apparatus itself can also be shaken by various environmental disturbances, such as

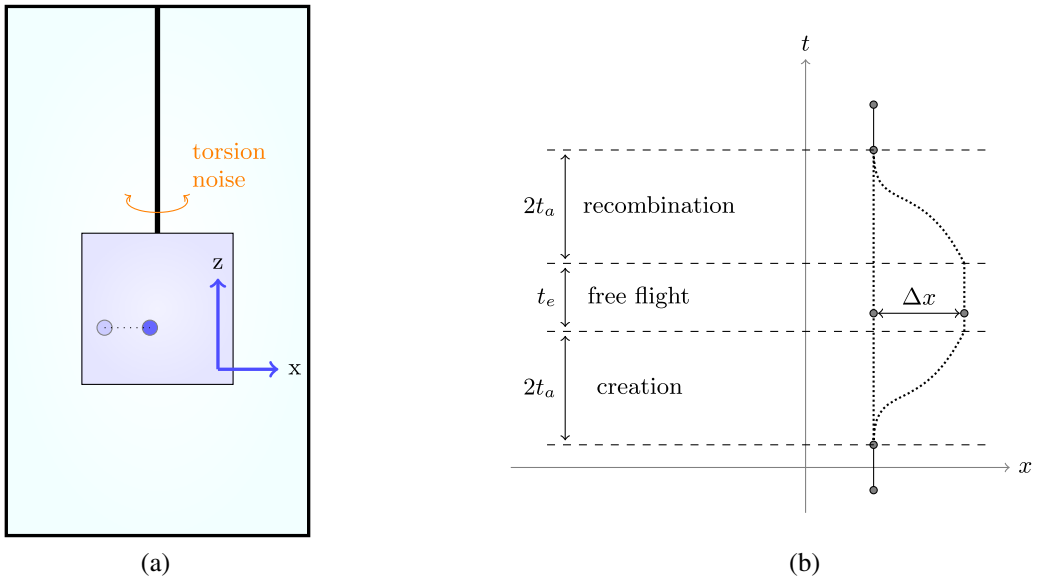

FIG. 1. (a) Experimental scheme and illustration of ITN. The matter-wave particle (filled circles) is placed inside the experimental box (square box), which is suspended by a thin wire (vertical bold line). The box can rotate around the z axis, while the interferometric protocol is performed along the horizontal x axis. ITN generates random torques on the experimental box (square box), placing it in noninertial rotational motion. The random noninertial rotational motion induces random relative phases, which can lead to dephasing and the loss of interferometric contrast. (b) The structure of a Stern-Gerlach interferometer with spin-1 [25]. The left path keeps the same position, while the right path accelerates and decelerates at a constant rate, resulting in a superposition size Δx. Such motion is achieved using a constant magnetic field gradient, i.e., $B(x) = B_0 + \eta x$, where the gradient η is positive during $0 \sim t_a$ and $3t_a + t_e \sim 4t_a + t_e$, while it is negative during $t_a \sim 2t_a$ and $2t_a + t_e \sim 3t_a + t_e$. During the intermediate free flight of duration t_e, the magnetic field is uniform and the right path does not accelerate. Such an asymmetrically shaped interferometer can be used to detect gravity gradients [21,34,35].

vibrations of mechanical supports and jitter caused by collisions of air molecules. These vibrations of the experimental apparatus are applied to the interferometer as noninertial forces, resulting in acceleration and rotation noises, affecting the interferometer's final phase, i.e., *residual acceleration noise* [34,35] and *inertial rotation noise*, which we investigate in this paper. Such noises can induce dephasing, which can be mitigated only by carefully controlling the experimental setup and its environment.

In this paper, we focus on the Stern-Gerlach interferometer with the configuration shown in Fig. 1(b), which can be achieved by a system with a spin-1 state and spin-0 state (embedded in an object) in a magnetic field with a constant gradient; see [21]. In particular, the system is prepared in a spin superposition of $|S=0\rangle$ and $|S=1\rangle$, say, $|\psi\rangle = 1/\sqrt{2}(|S=0\rangle + |S=1\rangle)$. At the same time, the external magnetic field has a linear spatial distribution on the x axis, i.e., $B(x) = B_0 + \eta x$, where the magnetic gradient η will flip several times to accelerate and decelerate the state $|S=1\rangle$.

Therefore, the acceleration of the $|S=1\rangle$ state is a constant $a_m = g\mu_B\eta$ during $0 \sim t_a$ and $3t_a + t_e \sim 4t_a + t_e$, and $a_m = -g\mu_B\eta$ during $t_a \sim 2t_a$ and $2t_a + t_e \sim 3t_a + t_e$, where $g = 2$ is the Lande factor and $\mu_B = 9.27 \times 10^{-24}$ J/T is the Bohr magneton.

In an ideal experiment (without any dephasing and decoherence), the final state of the system is

$$|\psi\rangle = \frac{1}{\sqrt{2}} e^{i\phi_{\text{global}}} (|S=0, L\rangle + e^{i\phi_{\text{diff}}} |S=1, R\rangle), \quad (1)$$

where ϕ_{global} is the global phase of the quantum state and ϕ_{diff} is the differential phase between two paths denoted as "L" and "R." The global phase does not have observable effects, while the differential phase ϕ_{diff} usually encodes the signal we want to extract. For example, ϕ_{diff} is related to the gravitation acceleration g for a gravimeter [43]. Another example is the QGEM experiment, which encodes information about the nature of gravity.

However, some classical noises like residual acceleration noise and ITN always exist. They will contribute some random phase $\delta\phi$ on ϕ_{diff}. Although $e^{i\delta\phi}$ itself is a pure phase, the ensemble average of such a random phase can lead to a damping factor, known as a dephasing effect. For convenience, $\delta\phi$ is supposed to follow a Gaussian distribution with a mean value of zero and a variance of $\Gamma \equiv \mathbb{E}[(\delta\phi)^2]/2$, and then the expectation value of the phase can be computed as

$$\mathbb{E}[e^{i\delta\phi}] = e^{-\mathbb{E}[(\delta\phi)^2]} \equiv e^{-\Gamma}, \quad (2)$$

where $\mathbb{E}[\cdot]$ is the ensemble average of random variables. Note that for a more general probability distribution of $\delta\phi$, one can also define a similar Γ to describe the dephasing effect [44]. Such a decay factor $e^{-\Gamma}$ will cause the loss of visibility of the interferometer. In particular, consider the ensemble average of the density matrix $\hat{\rho} = |\psi\rangle\langle\psi|$:

$$\mathbb{E}[\hat{\rho}] = \frac{1}{2}(|L\rangle\langle L| + |R\rangle\langle R| + \mathbb{E}[e^{i\delta\phi}]e^{2i\phi_{\text{diff}}}|R\rangle\langle L| + \mathbb{E}[e^{-i\delta\phi}]e^{-2i\phi_{\text{diff}}}|L\rangle\langle R|). \quad (3)$$

The off-diagonal terms decay exponentially with the damping given by the variance Γ. Consequently, the expectation value $\text{Tr}(\hat{W}\hat{\rho})$ of any witness operator $\hat{W}$ will also decay with respect to the factor $e^{-\Gamma}$.

For example, one can consider two applications of matter-wave interferometers for gravity experiments.

(1) The first application is the gravimeter based on a Nitrogen-vacancy center [43,45]. The gravitational acceleration g is proportional to the differential phase as $\phi_{\text{diff}} = 16\pi m g \Delta z/(\hbar\omega_0)$, where Δz is the superposition size along the z axis and $\omega_0 \sim 100$ kHz is the trapping frequency. Then, the phase fluctuation can cause a sensitivity loss on the measurement result of g, and one can obtain a constraint for Γ by the variance σ_g of δg as $\sqrt{\Gamma} = 16\pi m \sigma_g \Delta z/(\hbar\omega_0)$, as long as $\delta\phi_{\text{diff}}$ and δg follow Gaussian distributions. Choosing the values as $m \sim 10^{-16}$ kg and $\Delta z \sim 10^{-8}$ m [46], one may obtain a threshold as $\sqrt{\Gamma} < \sigma_g 10^7$ s^2/m. A common performance of gravimeters is $\sigma_g = 10^{-9} \sim 10^{-10} g$ [46], and one can choose the threshold of Γ as 10^{-6}.

(2) Another example is the QGEM experiment [34,37], which uses two interferometers coupled by gravity to investigate gravity-induced quantum entanglement. The witness $\hat{W}$ is proposed as the positive partial transpose witness, which, in the case of two qubits, provides a sufficient and necessary condition for entanglement based on the Peres-Horodecki criterion [47–49], which requires that the expectation value of the witness satisfies $\langle\hat{W}\rangle < 0$. As calculated in [37], the expectation value of the witness under the dephasing effect is $\langle\hat{W}\rangle = (1 - e^{-2\Gamma})/4 - e^{-\Gamma/2}\sin\phi_g$, and then the constraint on Γ is that $\Gamma/2 < e^{-\Gamma/2}\sin\phi_g \approx \phi_g$. The value of ϕ_g was estimated as $\phi_g \approx 0.015$ [34,50], and we choose a threshold $\Gamma = 0.01$ for further discussions on the values of parameters in this paper.

Dephasing, together with all other types of decoherence, can be also characterized by computing the purity:

$$\text{Tr}(\mathbb{E}[\hat{\rho}]^2) = \frac{1}{2}(1 + e^{-2\Gamma}) \approx 1 - \Gamma. \quad (4)$$

Note that the dephasing comes from the ensemble average of the density matrix. In particular, $\text{Tr}(\hat{\rho}^2)$ without the ensemble average still equals 1. We refer to Γ as the

dephasing factor in the following text. In the next section, we analyze the dephasing factor Γ caused by the ITN.

III. DEPHASING AS LINEAR RESPONSE TO INERTIAL TORSION NOISE

As is derived in Appendix A, the Lagrangian of the inertial torsion noise is given by

$$L_{\mathrm{ITN}} = \frac{1}{2} m \dot{\Theta}^2 x^2, \tag{5}$$

where m and x are the interferometer's mass and position and $\Theta(t)$ is the torsion angle of the suspended apparatus, i.e., the angle between the apparatus reference frame and the inertial reference frame.

The angle $\Theta(t)$ is assumed to be a stochastic Gaussian process, satisfying the following two properties:

$$\begin{aligned} \mathbb{E}[\Theta(t)] &= 0, \\ \mathbb{E}[\Theta(t_1)\Theta(t_2)] &= \int S_{\Theta\Theta}(\omega) \mathrm{e}^{-\mathrm{i}\omega(t_2-t_1)} \mathrm{d}\omega, \end{aligned} \tag{6}$$

where $S_{\Theta\Theta}(\omega)$ is the *power spectrum density* of $\Theta(t)$ and the second identity is known as the Wiener-Khinchin theorem. The PSD of Θ can be measured in the experiment. In this paper, we consider a specific source of fluctuation of Θ (e.g., the collision by gas molecules, which will be discussed in the next section).

As is proved in [51,52], the phase fluctuations due to noises are determined by the path integral of the corresponding Lagrangian of the noise along the unperturbed classical trajectories. Thus, the phase fluctuation is

$$\begin{aligned} \delta\phi &= \frac{1}{\hbar} \int L_{\mathrm{ITN}}[x_R(t)] - L_{\mathrm{ITN}}[x_L(t)] \mathrm{d}t \\ &= \frac{m}{2\hbar} \int \dot{\Theta}^2(t) \left(x_R^2(t) - x_L^2(t)\right) \mathrm{d}t, \end{aligned} \tag{7}$$

where $x_R(t)$ and $x_L(t)$ are the trajectories of the interferometer's two arms. Assuming the expectation value of $\delta\phi$ vanishes, the variance $\Gamma \equiv \mathbb{E}[(\delta\phi)^2]$ of the random phase can be regarded as the linear response of the interferometer to the torsion noise [34]:

$$\Gamma = \frac{m^2}{4\hbar^2} \int S_{\dot{\Theta}^2\dot{\Theta}^2}(\omega) F(\omega) \mathrm{d}\omega, \tag{8}$$

where $S_{\dot{\Theta}^2\dot{\Theta}^2}(\omega)$ is the PSD of the ITN. According to the Wiener-Khinchin theorem, the PSD is the Fourier transform of the autocorrelation function of the torsion noise,

$$S_{\dot{\Theta}^2\dot{\Theta}^2}(\omega) = \int \mathrm{E}[\dot{\Theta}^2(t_0)\dot{\Theta}^2(t_0+\tau)] \mathrm{e}^{\mathrm{i}\omega\tau} \mathrm{d}\tau. \tag{9}$$

Note that $S_{\dot{\Theta}^2\dot{\Theta}^2}(\omega)$ has units $\mathrm{Hz}^4/\mathrm{Hz}$, where Hz^4 comes from the square of $\dot{\Theta}^2$ and the denominator Hz describes the density of frequency space. The $F(\omega)$ in Eq. (8) has units $\mathrm{m}^4\,\mathrm{s}^2$ and is given by

$$F(\omega) = \left| \int (x_R^2(t) - x_L^2(t)) \mathrm{e}^{\mathrm{i}\omega t} \mathrm{d}t \right|^2. \tag{10}$$

Equation (8) describes the input-output relation of the interferometer and only depends on the trajectories of the two arms, so it can be called the *transfer function* of the interferometer [35]. For the interferometer in Fig. 1(b), the left arm is static, $x_L(t) \equiv 0$, and the right arm $x_R(t)$ is described by a piecewise function consisting of several quadratic functions of t because the acceleration is $\pm a_m$ for the different time range. Then, the transfer function can be computed as

$$\begin{aligned} F(\omega) = 16 \frac{a_m^4}{\omega^{10}} \Bigg[& 6\omega t_a \cos\left(\omega\left(t_a + \frac{t_e}{2}\right)\right) \\ & + (\omega^2 t_a^2 + 3) \sin\frac{\omega t_e}{2} - 3\sin\left(\omega\left(2t_a + \frac{t_e}{2}\right)\right) \\ & - \omega^2 t_a^2 \sin\left(\omega\left(t_a + \frac{t_e}{2}\right)\right)\Bigg]^2. \end{aligned} \tag{11}$$

Figure 2 shows the transfer function with the parameters chosen as $t_a = 0.25$ s, $t_e = 0$ s, and $a_m = 1.8 \times 10^{-4}$ m/s^2, where $a_m = g\mu_B\eta/m_0$ with the magnetic field gradient $\eta = 10^4$ T/m and the mass of the interferometer $m_0 = 10^{-15}$ kg.

As is shown in Fig. 2, $F(\omega)$ tends to a constant $C \sim (\Delta x)^4 T^2 \sim 10^{-20}$ m^4 s^2 in the low-frequency limit, where $\Delta x = a_m t_a^2 = 11.2$ μm and $T = 4t_a + t_e$ are the superposition size and total experiment time. Because the factor $\mathrm{e}^{i\omega t} \to 1$ in the low-frequency limit $\omega \to 0$ and the superposition size Δx is an upper bound for $x_R(t)$ when $x_L(t) \equiv 0$, $F(\omega)$ in (10) can be approximated in the low-frequency region as

$$F(\omega) \sim \left| \int (\Delta x)^2 \mathrm{d}t \right|^2 = (\Delta x)^4 T^2. \tag{12}$$

In the high-frequency limit, $F(\omega)$ decreases as ω^{-6}. In particular, the trajectory $x_R(t)$ can be generally expanded as a Taylor series of t with the leading order $x_R(t) \sim t$, so $x_R^2(t) \sim t^2$; then, the leading order of $F(\omega)$ can be estimated according to (10) as

$$F(\omega) \sim \left| \int t^2 \mathrm{e}^{i\omega t} \mathrm{d}t \right|^2 \sim (\omega^{-3})^2 = \omega^{-6}. \tag{13}$$

Combining the low-frequency and high-frequency behaviors of $F(\omega)$, one can use the Heaviside step function

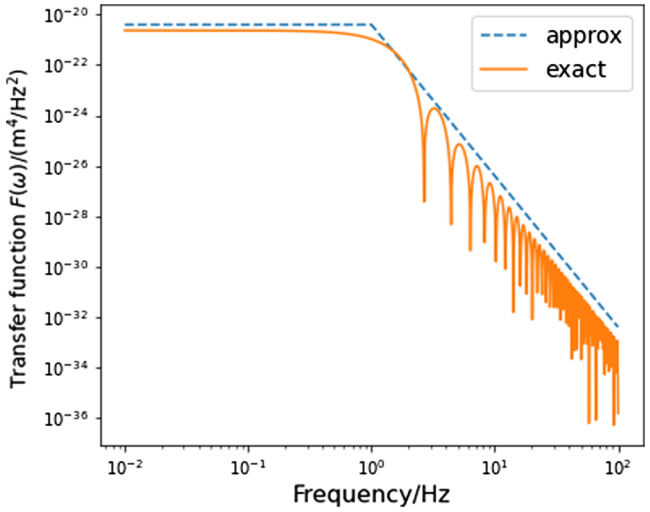

FIG. 2. Transfer function of the interferometer illustrated in Fig. 1(b) as a function of the frequency $f = \omega/(2\pi)$. The time parameters are $t_a = 0.25$ s and $t_e = 0$ s. The magnetic field gradient η is chosen as 10^4 T/m and the mass of the interferometer is chosen as 10^{-15} kg. The resulting acceleration $a_m = 1.8 \times 10^{-4}$ m/s^2 produces the maximum superposition size $\Delta x = a_m t_a^2 = 11.2$ μm. As is shown, the transfer function tends to a constant $C \sim (\Delta x)^4 T^2 \sim 10^{-20}$ m^4 s^2 at low frequencies and decreases as ω^{-6} at high frequencies. The approximate transfer function from Eq. (14) (dashed blue line) captures the behavior of the transfer function from Eq. (11) (orange line).

$\theta(\cdot)$ to approximately describe $F(\omega)$ as

$$F(\omega) \approx (\Delta x)^4 T^2 \left(\theta\left(\frac{2\pi}{T} - \omega\right) + \left(\frac{2\pi}{T\omega}\right)^6 \theta\left(\omega - \frac{2\pi}{T}\right)\right). \tag{14}$$

IV. POWER SPECTRUM DENSITY OF INERTIAL TORSION NOISE

In this section, we analyze the inertial torsion noise caused by the thermal motion of gas molecules surrounding the experimental box.

According to the convolution theorem, the PSD of ITN is the self-convolution of the PSD of the random motion of the suspended apparatus,

$$S_{\dot\Theta^2\dot\Theta^2}(\omega) = S_{\dot\Theta\dot\Theta}(\omega) * S_{\dot\Theta\dot\Theta}(\omega), \tag{15}$$

where $S_{\dot\Theta\dot\Theta}(\omega)$ is the PSD of $\dot\Theta$. In frequency space, there is a correspondence that $\dot\Theta \sim i\omega\Theta$, so the PSD of $\dot\Theta(t)$ is

$$S_{\dot\Theta\dot\Theta}(\omega) = \omega^2 S_{\Theta\Theta}(\omega). \tag{16}$$

As is shown in Fig. 1(a), the rotational motion of the experimental box can be modeled as a torsion pendulum, which follows a generalized Langevin equation

$$\ddot\Theta = -\Omega_{\rm rot}^2 \Theta - \gamma\dot\Theta + \sqrt{A}\Theta_{\rm in}(t). \tag{17}$$

The input random noise term $\Theta_{\rm in}(t)$ is a unit delta-correlated stationary Gaussian process with zero mean, satisfying $\mathbb{E}[\Theta_{\rm in}(t)] = 0$ at any time t, and $\mathbb{E}[\Theta_{\rm in}(t_1)\Theta_{\rm in}(t_2)] = \delta(t_1 - t_2)$. The amplitude of the external noise $\sqrt{A}$[1] and the dissipation rate γ are determined by the experiment. The intrinsic torsion frequency is given by [53]

$$\Omega_{\rm rot} = \sqrt{\frac{\kappa}{I}} = \sqrt{\frac{\pi \mathbb{G} d^4}{32 l I}}, \tag{18}$$

where I is the moment of inertia of the experiment box and $\kappa = \sqrt{\pi \mathbb{G} d^4/32l}$ is the torsion constant. $\mathbb{G}$ is the shear modulus of the material of the suspension wire, and d and l are the diameter and length of the wire. The size and mass of the experiment box can be built up as $10^{-1} \sim 10^0$ m and $10^1 \sim 10^2$ kg, so the moment of inertia I can be estimated as $10^0 \sim 10^2$ kg $\cdot$ m^2. The parameters of the suspension wire are around $d = 10^{-3} \sim 10^{-2}$ m, $l = 10^0 \sim 10^1$ m, and $\mathbb{G} \sim 10^{10}$ Pa, and thus the intrinsic frequency $\Omega_{\rm rot}$ of the torsion pendulum is around $10^{-2} \sim 10^1$ Hz.

For example, if the experiment box is built with a size $L = 0.6$ m and mass $M = 30$ kg, then the moment of inertia is $I = ML^2/6 = 1.8$ kg $\cdot$ m^2. If the suspension wire is set as $d = 5 \times 10^{-3}$ m and $l = 5$ m, and the shear modulus is chosen as $\mathbb{G} = 7.93 \times 10^{10}$ Pa for steel [54], then the intrinsic torsion frequency is $\Omega_{\rm rot} \approx 0.735$ Hz according to Eq. (18).

Based on the dynamical equation (17) of the experiment box, the power spectrum for Θ is[2]

$$S_{\Theta\Theta}(\omega) = \frac{A}{(\Omega_{\rm rot}^2 - \omega^2)^2 + \gamma^2\omega^2}. \tag{19}$$

One may do a Monte Carlo simulation of the Langevin equation given in Eq. (17), shown as the upper figure of Fig. 3, and calculate the corresponding PSD by fast Fourier transform (FFT), where a Hanning window is added to avoid the spectral leakage, shown as the lower

[1]Note that A has units Hz^4/Hz. This is because the term $\sqrt{A}\Theta_{\rm in}(t)$ has dimensions [T^{-2}], where $\Theta_{\rm in}(t)$ has dimensions [T$^{-1/2}$].

[2]Here we used the result $S_{\rm in}(\omega) \equiv |\Theta_{\rm in}(\omega)|^2/T_{\rm tot} = 1$, which can be obtained through the autocorrection condition $\mathbb{E}[\Theta_{\rm in}(t_1)\Theta_{\rm in}(t_2)] = \delta(t_1 - t_2)$ and the Wiener-Khinchin theorem that

$$\frac{|\Theta_{\rm in}(\omega)|^2}{T_{\rm tot}} = \int \mathbb{E}[\Theta_{\rm in}(t)\Theta_{\rm in}(t+\tau)]e^{i\omega\tau}d\tau = \int \delta(\tau)e^{i\omega\tau}d\tau = 1.$$

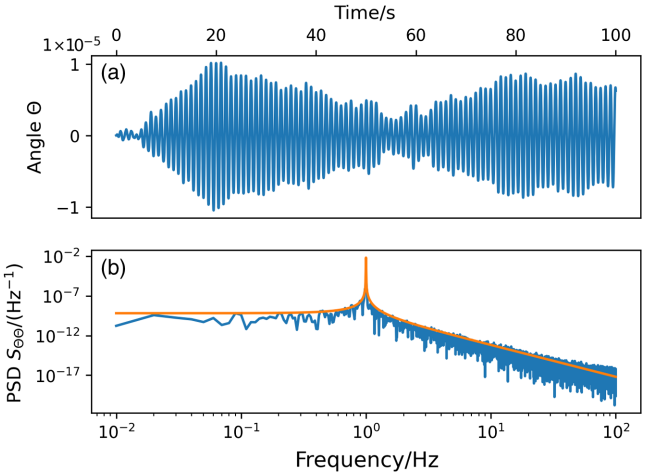

FIG. 3. Monte Carlo simulation for the motion of the box. (a) Simulated time trace of Eq. (C1). (b) The PSD $S_{\Theta\Theta}(\omega)$ in the lower plot is computed by FFT. Theoretically, the PSD is a Lorentzian distribution, which fits the simulation result well. The intrinsic frequency $\Omega_{\rm rot}$ is chosen as $2\pi \times 1$ Hz, the damping rate γ is chosen as 10^{-10} Hz, and the noise amplitude $\sqrt{A}$ is chosen as 10^{-3} Hz^2/Hz.

figure of Fig. 3. We find that the analytic result (19) matches well with the numerical result.

Since the PSD of ITN is the self-convolution of $S_{\dot\Theta\dot\Theta}(\omega)$ according to Eq. (15), one can compute the PSD of the ITN driven by the external noise with the PSD given by Eq. (19) as

$$S_{\dot\Theta^2\dot\Theta^2}(\omega) = A^2 \frac{4\omega^4 + 4(\gamma^2 - 3\Omega_{\rm rot}^2)\omega^2 + 16\Omega_{\rm rot}^4}{\gamma(\omega^2+\gamma^2)(4\gamma^2\omega^2 + (\omega^2 - 4\Omega_{\rm rot}^2)^2)}. \quad (20)$$

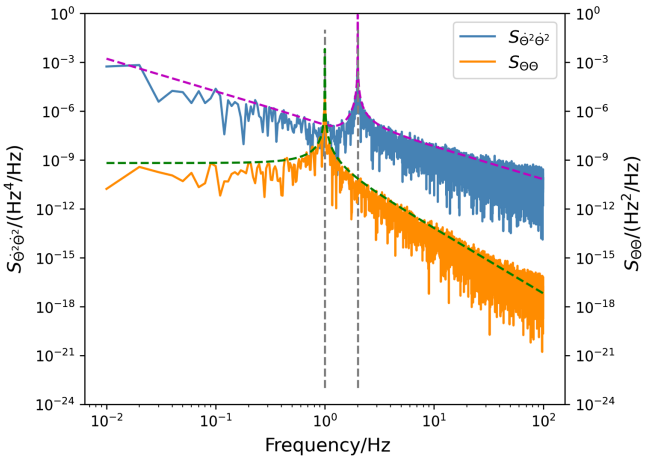

FIG. 4. PSD of ITN $S_{\dot\Theta^2\dot\Theta^2}(\omega)$ and angular motion PSD $S_{\Theta\Theta}(\omega)$. The parameters are chosen as $\Omega_{\rm rot} = 2\pi \times 1$ Hz, $\gamma = 10^{-10}$ Hz, $I = 10$ kg $\cdot$ m^2, and $\sqrt{A} = 10^{-3}$ Hz$^2/\sqrt{\rm Hz}$. The peak frequency of $S_{\dot\Theta^2\dot\Theta^2}(\omega)$ is doubled compared to $S_{\Theta\Theta}(\omega)$, as expected when computing the square of the noise. The dashed green and purple lines show that the theoretical expressions in Eqs. (19) and (20) fit well the simulated PSDs.

The detailed mathematical steps are summarized in Appendix B. Figure 4 shows the analytical result and numerical simulation of both $S_{\Theta\Theta}(\omega)$ and $S_{\dot\Theta^2\dot\Theta^2}(\omega)$.

The asymptotic behavior of the PSD of ITN is different from the $S_{\Theta\Theta}(\omega)$. In the low-frequency limit, $S_{\dot\Theta^2\dot\Theta^2}(\omega)$ behaves like $1/(\omega^2 + \gamma_{\rm rot}^2)$ and tends to a constant A^2/γ. In the high-frequency region, $S_{\dot\Theta^2\dot\Theta^2}(\omega)$ decreases as ω^{-2} according to the analytic result (20).

There is also a peak of the PSD of ITN, of which the resonance frequency translates from $\Omega_{\rm rot}$ to $2\Omega_{\rm rot}$, which is a common property for a squared noise.[3] In a small-damping limit $\gamma_{\rm rot} \ll \Omega_{\rm rot}$, the peak value of $S_{\dot\Theta^2\dot\Theta^2}(\omega)$ is

$$S_{\dot\Theta^2\dot\Theta^2}(2\Omega_{\rm rot}) \approx \frac{A^2}{2\gamma^3}. \quad (21)$$

It is notable that

$$S_{\dot\Theta^2\dot\Theta^2}(2\Omega_{\rm rot} \pm \gamma) \approx \frac{A^2}{4\gamma^3}. \quad (22)$$

So, the frequencies at which the PSD is equal to the half-peak value are $\omega = 2\Omega_{\rm rot} \pm \gamma$ and the corresponding FWHM is 2γ. The ratio between the bandwidth and peak value is known as the quality factor (Q-factor) of the PSD, which characterizes the sharpness of the peak. Then, the Q-factor of $S_{\dot\Theta^2\dot\Theta^2}(\omega)$ is

$$Q_{\rm ITN} = \frac{2\Omega_{\rm rot}}{2\gamma} = \frac{\Omega_{\rm rot}}{\gamma}, \quad (23)$$

which is exactly the same as the Q-factor of $S_{\Theta\Theta}(\omega)$.

V. DEPHASING FACTOR AND EXPERIMENTAL PARAMETER CONSTRAINTS

Based on the result of the transfer function in Eq. (11) or Eq. (14), and the PSD (20) of the inertial torsion noise, the dephasing factor Γ can be computed through the integral

[3]This property can be understood as follows. Since $S_{\dot\Theta\dot\Theta}$ has a peak at $\Omega_{\rm rot}$, it can be written as a δ function plus some small function $o(\omega)$,

$$S_{\dot\Theta\dot\Theta}(\omega) = S_0\delta(\omega - \Omega_{\rm rot}) + o(\omega),$$

where S_0 is the amplitude of the peak. Then, the self-convolution of $S_{\dot\Theta\dot\Theta}$ gives

$$\begin{aligned} S_{\dot\Theta^2\dot\Theta^2}(\omega) &= S_0^2 \int \delta(\omega' - \Omega_{\rm rot})\delta(\omega - \omega' - \Omega_{\rm rot})d\omega' + o'(\omega) \\ &= S_0^2\delta(\omega - 2\Omega_{\rm rot}) + o'(\omega), \end{aligned}$$

which means that the peak position is located at $2\Omega_{\rm rot}$. In Appendix B, we offer another method to understand this property in the time domain.

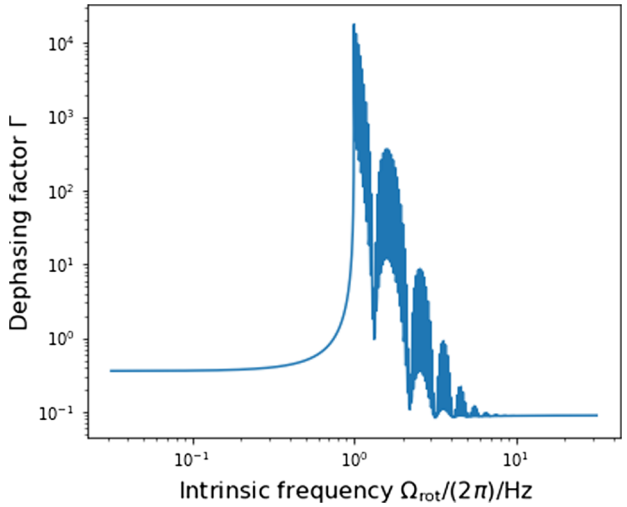

FIG. 5. Dephasing factor Γ as a function of the intrinsic torsion frequency Ω_{rot}. The parameters are chosen as $m_0 = 10^{-15}$ kg, $\eta = 10^4$ T/m, $t_a = 0.25$ s, and $t_e = 0$ s for the interferometer, and $\gamma = 10^{-10}$ Hz, $I = 10\ \mathrm{kg}\cdot\mathrm{m}^2$, and $A = 10^{-10}$ Hz^4/Hz for the PSD of ITN. There is a resonance between the ITN and the transfer function with the first dominant peak at $\Omega_{rot} \sim 2\pi/T_{tot} \sim 2\pi \times 1$ Hz, and additional smaller peaks visible in the range up to 10. In the low-frequency and high-frequency limits, the dephasing factor Γ is approximately independent of the intrinsic frequency Ω_{rot}.

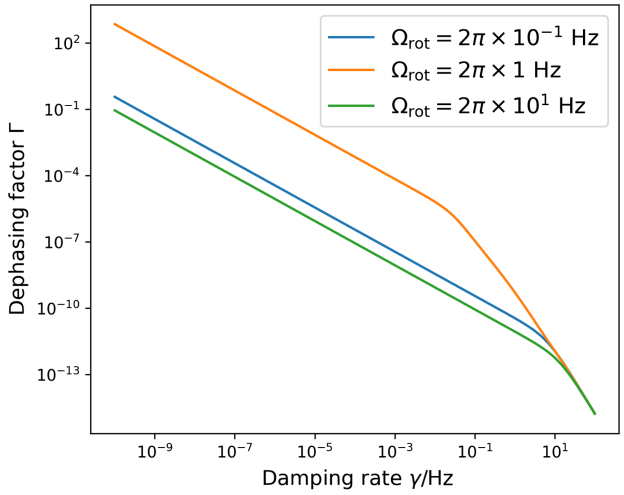

FIG. 6. Relationship between Γ and the damping factor γ for a fixed amplitude $A = 10^{-10}$ Hz^3. The transfer function is given in Eq. (11) with parameters $t_a = 0.25$ s and $t_e = 0$ s. Three different Ω_{rot} are chosen as the low rotation frequency limit, the high rotation frequency limit, and the resonance frequency condition $\Omega_{rot} \sim 2\pi/T = 2\pi$ Hz. Γ is proportional to γ^{-1} when $\gamma \ll \Omega_{rot}$, while it decreases at a speed of γ^{-3} in the overdamped region.

in Eq. (8). Note that the analytic solution to the integral is very complicated, so we compute it numerically. It is noteworthy that a resolution of $\omega_{min} = 2\pi/T_{tot}$ exists as a cutoff in frequency space for the numerical calculation. Physically, this cutoff indicates that a low-frequency signal or noise will not be measurable by the experiment if the total experiment time is shorter than a single period of such signal or noise.

Figure 5 shows the dependence of Γ on the intrinsic torsion frequency Ω_{rot} of the experimental apparatus, where the parameters of $F(\omega)$ are chosen as $m_0 = 10^{-15}$ kg, $t_a = 0.25$ s, and $t_e = 0$ s, and the parameters of $S_{\dot\Theta^2\dot\Theta^2}(\omega)$ are A $= 10^{-10}$ Hz^4/Hz and $\gamma = 10^{-10}$ Hz. As is shown, there is a resonance between the ITN and the transfer function near $\Omega_{rot} \sim 2\pi/T_{tot} = 2\pi \times 1$ Hz and some harmonic resonances. Note that, near the resonance peak, the precision of the numerical calculation is limited because the value is highly related to the sample points in frequency space.

When Ω_{rot} is much larger than $2\pi \times 10^0$ Hz, Γ becomes approximately independent of Ω_{rot}. On the other hand, when Ω_{rot} is much smaller than $2\pi \times 10^{-1}$ Hz, the peak will be below the frequency cutoff ω_{min}, so the dephasing factor will be tiny. For an actual experiment, the low intrinsic frequency limit is expected, so the parameters d, l, $\mathbb{G}$, and I in (18) have to be carefully designed to ensure that Ω_{rot} is much smaller than the resonance frequency $2\pi/T$ of the interferometer.

Figure 6 shows the dependence of Γ on the damping rate γ. As is shown, when the damping rate is very low, i.e., $\gamma \ll \Omega_{rot}$, the dephasing parameter Γ is approximately proportional to γ^{-1} due to the γ^{-1} factor in (20).

However, when γ increases after a critical point $\gamma \sim \Omega_{rot}$, the dephasing Γ is approximately γ^{-3}. This is because the PSD of ITN in the high damping rate limit $\gamma \gg \Omega_{rot}$ is approximately

$$S_{\dot\Theta^2\dot\Theta^2}(\omega) \approx A^2 \frac{4\omega^4 + 4\gamma_{rot}^2\omega^2}{\gamma(\omega^2+\gamma^2)(\omega^4+4\gamma^2\omega^2)} \sim \frac{A^2}{\gamma^3}. \tag{24}$$

Physically, this can be interpreted as an overdamped oscillator. In particular, the apparatus' dynamical equation in Eq. (17) describes a damped oscillator under a randomly driven force. When the damping rate is larger than a critical value $\gamma > \Omega_{rot}/2$, the system decays with no oscillation, known as overdamped. In the overdamped region, as the damping rate increases, the system decays to the equilibrium faster, so the random force term affects the system less. Finally, the dephasing parameter Γ decreases as the damping rate γ increases.

Figure 7 shows the dependence of the dephasing parameter Γ concerning different damping rates γ and torsion noise amplitude A, where the parameters are chosen as $t_a = 0.25$ s, $t_e = 0$ s, and $\Omega_{rot} = 2\pi \times 1$ Hz. As is shown, Γ increases as A increases or γ decreases. As discussed in Sec. II, the gravimeter and QGEM experiments require an upper bound on Γ of 10^{-6} and 0.01; then, A and γ should be chosen in the region on the left side of the dotted and dashed critical line, respectively, in the figure.

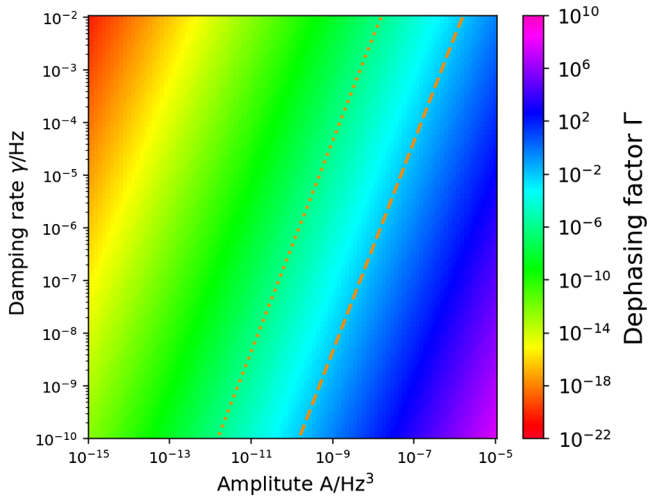

FIG. 7. Dephasing parameter Γ with respect to different damping rates γ and torsion noise amplitudes A. The transfer function is given by Eq. (11) with parameters $t_a = 0.25$ s and $t_e = 0$ s, and the intrinsic frequency is chosen as $\Omega_{\rm rot} = 2\pi \times 1$ Hz. Γ is required to be smaller than some thresholds in different situations; then, the parameters should be chosen on the left side of the critical lines in the figure, where the dotted and dashed lines represent $\Gamma = 10^{-6}$ and $\Gamma = 0.01$ for gravimeter and QGEM experiments, respectively.

Figure 8 shows the upper bound of the torsion noise amplitude A to obtain a dephasing parameter Γ smaller than 0.01, where the parameters are also chosen as $t_a = 0.25$ s and $t_e = 0$ s. Since Γ is proportional to A^2, one can also use Fig. 8 to analyze other thresholds of Γ by multiplying by a factor of A. For example, one can analyze the case

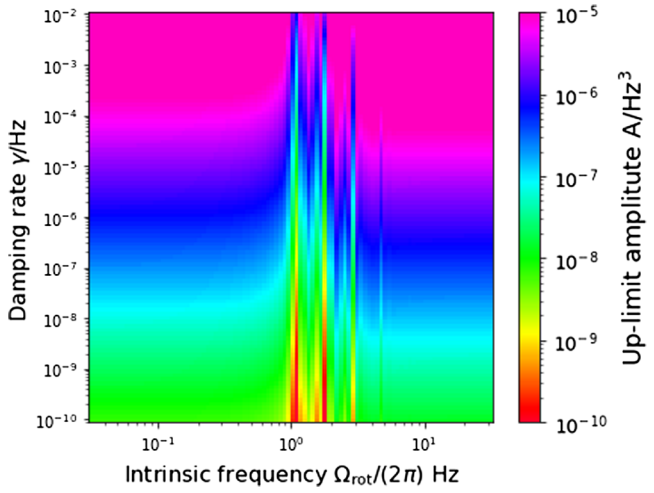

FIG. 8. Upper bound of the amplitude A assuming the value of the dephasing to be $\Gamma = 0.01$. The transfer function is given by Eq. (11) with parameters $t_a = 0.25$ s and $t_e = 0$ s. Near the resonance region $\Omega_{\rm rot} \sim 2\pi/T_{\rm tot} = 2\pi \times 1$ Hz and its harmonic resonance $\Omega_{\rm rot} \sim 2n\pi/T_{\rm tot}$ (with n a positive integer), the upper bound of A becomes more constrained. On the other hand, the requirements on A relax outside the resonance region.

$\Gamma < 10^{-6}$ for gravimeters by multiplying 10^{-2} to the upper bound of A.

As is shown, the restriction on the upper bound of A is very stringent near the resonance region $\Omega_{\rm rot} \sim 2\pi/T_{\rm tot} = 2\pi \times 1$ Hz and its harmonic resonance $\Omega_{\rm rot} \sim 2n\pi/T_{\rm tot}$ (with n a positive integer). In particular, A has to be smaller than 10^{-10} Hz^3 for $\gamma = 10^{-10}$ Hz, and it has to be smaller than 10^{-8}Hz^3 for $\gamma = 10^{-2}$ Hz. On the other hand, the value of A is less severely constrained outside the resonance region. For a damping rate larger than 10^{-4} Hz, A can be larger than 10^{-5} Hz^3.

In a recent simulation work [55], a relationship between the torsion noise amplitude A and the superposition size Δx was obtained as $\Delta x A \sim 10^{-11}$ m $\cdot$ Hz^3. Since the superposition size discussed in this paper is $\Delta x = a_m t_a^2 = 11.2$ μm, the noise amplitude is $A \sim 10^{-6}$ Hz^3, which is smaller than the restricted bound $A_{\rm bound} \sim 10^{-5}$ Hz^3. In conclusion, as long as the damping rate is designed to be larger than 10^{-4} Hz and the intrinsic frequency $\Omega_{\rm rot}$ is designed outside the resonance region, the dephasing parameter Γ of the interferometer will be smaller than 0.01.

VI. SUMMARY

In this paper, we investigated ITN in the context of matter-wave interferometry, and some of our highlights and conclusions are summarized below.

In Sec. II, we explained the physical interpretation of the ITN and briefly reviewed the dephasing effect of generic noises on matter-wave interferometers. The key point is that the ensemble average of a random phase implies a decay factor $\mathbb{E}[e^{i\delta\phi}] = e^{-\Gamma}$ on the off-diagonal terms of the density matrix, where the dephasing parameter is exactly the variance of the noise $\Gamma = \mathbb{E}[(\delta\phi)^2]$.

In Sec. III, we pointed out that the decay factor Γ can be regarded as a linear response of the interferometer to the ITN. In particular, Γ can be formulated as the PSD of the noise $S_{\dot\Theta^2\dot\Theta^2}(\omega)$ multiplying a transfer function $F(\omega)$ in frequency space. Remarkably, $F(\omega)$ only relies on the trajectories of the two arms of the interferometer and is independent of the noise. In the rest of Sec. III, some asymptotic features of $F(\omega)$ were discussed, and the exact and approximate results for a certain interferometer are shown in Fig. 2.

In Sec. IV, we modeled the torsion noise by a generalized Langevin equation (17), which implies the PSD $S_{\Theta\Theta}(\omega)$ in (19). Then, the PSD of the ITN $S_{\dot\Theta^2\dot\Theta^2}(\omega)$ is the self-convolution of $S_{\dot\Theta\dot\Theta}(\omega)$ according to the convolution theorem, where the mathematical details are summarized in Appendix B. It is remarkable that the peak position of $S_{\dot\Theta^2\dot\Theta^2}(\omega)$ is doubled compared to $S_{\dot\Theta\dot\Theta}(\omega)$ because of properties of self-convolution, while the Q-factor of $S_{\dot\Theta^2\dot\Theta^2}(\omega)$ remains the same as $S_{\dot\Theta\dot\Theta}(\omega)$.

In Sec. V, we scanned parameters theoretically and found the following major features. First, Γ increases significantly near the resonance region $\Omega_{\rm rot} = 2n\pi/T_{\rm tot}$.

Next, Γ decreases proportionally to the damping rate γ^{-1} in the underdamped region, while it decreases with γ^{-3} in the overdamped region. Finally, if Γ is required to be smaller than 0.01, then the constraints on the parameters A, γ, and $\Omega_{\rm rot}$ are as shown in Fig. 8, and A is tolerant up to 10^{-5} Hz^3 if $\gamma > 10^{-4}$ Hz and $\Omega_{\rm rot}$ is outside the resonance region.

ACKNOWLEDGMENTS

M. W. would like to thank the China Scholarship Council (CSC) for financial support. M. T. would like to acknowledge funding from ST/W006227/1. S. B. thanks EPSRC grants EP/R029075/1, EP/X009467/1, and ST/W006227/1. A. M. and S. B.'s research is funded by the Gordon and Betty Moore Foundation through Grant No. GBMF12328, DOI 10.37807/GBMF12328. This material is based upon work supported by Alfred P. Sloan Foundation under Grant No. G-2023-21130. M. T. acknowledges funding from the Slovenian Research and Innovation Agency (ARIS) under contracts N1-0392, P1-0416, SN-ZRD/22-27/0510 (RSUL Toroš).

APPENDIX A: LAGRANGIAN OF INERTIAL TORSION NOISE

In this appendix, we derive the Lagrangian in Eq. (5) that gives rise to ITN. The basic idea is first to construct the metric in the comoving reference frame of the experimental apparatus (Appendix A 1), and then to compute the Lagrangian of the test mass in the nonrelativistic limit (Appendix A 2).

1. Rotating Fermi normal coordinates

To construct the coordinate system near the experiment, one can choose the worldline of the center of the experimental box as a fiducial time-like curve in the spacetime manifold. Based on this worldline, one can construct the Fermi normal coordinates of the spacetime using the method of the Fermi-Walker transport. Under these coordinates, the metric can be generally written as [56]

$$\begin{aligned} \mathrm{d}s^2 = &-\left[\left(1+\frac{a^b x'_b}{c^2}\right)^2 + R_{0c0d}x'^c x'^d\right]c^2\mathrm{d}t'^2 \\ &-\frac{2}{3}R_{0cbd}x'^c x'^d c\mathrm{d}t'\mathrm{d}x^b \\ &+\left(\delta_{bc}-\frac{1}{3}R_{bdce}x'^d x'^e\right)\mathrm{d}x'^b\mathrm{d}x'^c, \end{aligned} \tag{A1}$$

where the indices a, b, c, $d = 1, 2, 3$ represent the spacial coordinates. In the following, we neglect the linear acceleration terms $\sim a^b$ and the Riemann tensor terms $\sim R_{abcd}$ such that the metric in Eq. (A1) reduces to the Minkowski spacetime metric in Cartesian coordinates.

To obtain the metric in a rotating reference frame, we have to make an additional transformation. Rotations along the z axis can be described by the time-dependent angle $\theta(t)$, such that the coordinates in the rotating frame are described by

$$\begin{cases} t = t', \\ x = x'\cos\theta(t) + y'\sin\theta(t), \\ y = -x'\sin\theta(t) + y'\cos\theta(t), \\ z = z', \end{cases} \tag{A2}$$

where we recall that the primed symbols represent the coordinates in the inertial (nonrotating) frame (see Fig. 9).

To compute the metric in the rotating coordinates, one can proceed in several ways. For example, one way to simplify the calculation is to write the transformation between (x, y) and (x', y'), as well as between $(\mathrm{d}x, \mathrm{d}y)$

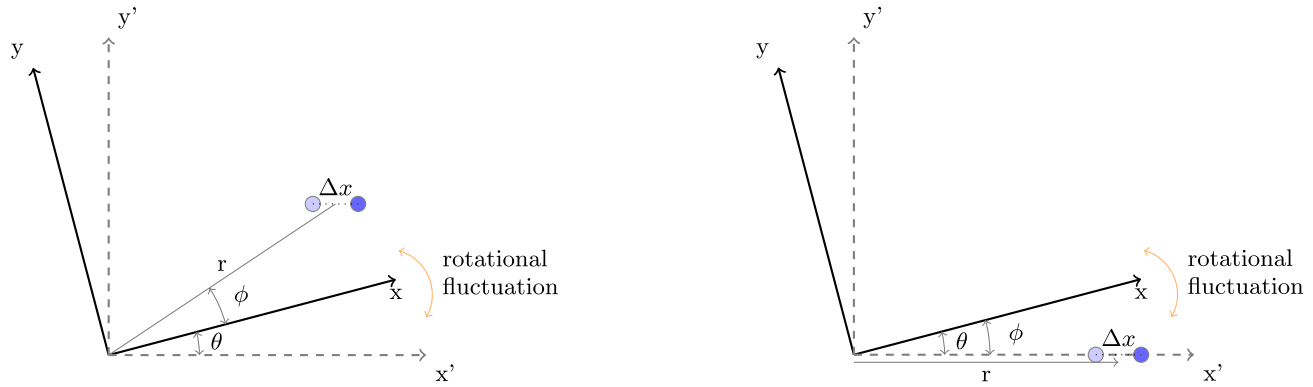

FIG. 9. Illustration of the inertial reference frame (labeled as x' and y') and the rotating reference frame (labeled as x and y), which is comoving with the experimental equipment. For simplicity, we assume that the interferometric axis (line segment connecting the filled circles) is aligned with the x' axis of the inertial frame. (a) General case when the interferometric particle is placed at an angle $\phi + \theta$ with respect to the inertial reference frame. ϕ denotes its polar coordinate in the rotating reference frame and θ is the angle between the inertial and rotating reference frames. (b) Special case when the interferometric axis coincides with the x' axis of the inertial reference frame. In this case, the two angles ϕ and θ defined in (a) have the simple relationship $\phi = -\theta$.

and (dx', dy'), in matrix form. However, here we offer an alternative method by exploiting the complex notation. The basic idea is to introduce a complex coordinate $w = x + iy$, and then the complex conjugate is $\bar{w} = x - iy$ and the differentials are

$$dw = dx + i dy, \qquad d\bar{w} = dx - i dy, \tag{A3}$$

with analogous expressions for the primed variables. This is a common trick to deal with 2D problems, because one can always construct a complex structure on a 2D surface through its metric to become a Riemann surface. For pedagogical material, see Chapter 7 of [57].

The rotation transformation from Eq. (A2), as well as its inverse, can be simply written as

$$w = w' e^{i\theta(t)}, \qquad w' = w e^{-i\theta(t)}, \tag{A4}$$

where we have omitted the t and z coordinate transformation for brevity. We find that the differential forms are

$$\begin{aligned} dw' &= e^{-i\theta} dw' - i\dot{\theta} w' e^{-i\theta} dt, \\ d\bar{w}' &= e^{i\theta} d\bar{w}' + i\dot{\theta}\bar{w}' e^{i\theta} dt. \end{aligned} \tag{A5}$$

The considered terms $dx'^2 + dy'^2 = dw' d\bar{w}'$ in the original Fermi normal coordinates from Eq. (A1) transform to

$$\begin{aligned} dw' d\bar{w}' &= (e^{-i\theta} dw - i\dot{\theta} w e^{-i\theta} dt)(e^{i\theta} d\bar{w} + i\dot{\theta}\,\bar{w}\, e^{i\theta} dt) \\ &= dw d\bar{w} - i\dot{\theta}(w d\bar{w} - \bar{w} dw) dt + \dot{\theta}^2 w\bar{w} dt^2 \\ &= dx^2 + dy^2 + 2\dot{\theta}(-x dy + y dx) dt \\ &\quad + \dot{\theta}^2 (x^2 + y^2) dt^2, \end{aligned} \tag{A6}$$

which then immediately give the transformed metric in the rotating reference frame,

$$\begin{aligned} ds^2 = &-(c^2 - \dot{\theta}^2(x^2 + y^2)) dt^2 + 2\dot{\theta}(-x dy + y dx) dt \\ &+ dx^2 + dy^2. \end{aligned} \tag{A7}$$

2. Lagrangian of inertial torsion noise

The Lagrangian of a point-like massive object is given by $L = -mc^2\sqrt{-ds^2/(c^2 dt^2)}$. Using the metric in Eq. (A7) and taking the nonrelativistic limit $v_x, v_y \ll c$ (with $v_x \equiv dx/dt$, $v_y \equiv dy/dt$), we find that the Lagrangian is

$$L = -\frac{1}{2} m\dot{\theta}^2 (x^2 + y^2) + m\dot{\theta}(-x v_y + v_x y), \tag{A8}$$

where we have omitted the constant term mc^2 and the kinetic energy term $1/2 m(v_x^2 + v_y^2)$. The term $-\frac{1}{2} m\dot{\theta}^2(x^2 + y^2)$ describes the centrifugal force. In particular, according to the Euler-Lagrange equation $\frac{d}{dt}\left(\frac{\partial L}{\partial \dot{x}_j}\right) - \frac{\partial L}{\partial x_j} = 0$, this term gives the centrifugal force $\vec{F}_{\text{cent}} = m\dot{\theta}^2 \vec{r}$. The term $m\dot{\theta}(-x v_y + v_x y)$ will give two forces, $-2m\vec{r} \times \dot{\vec{\theta}}$ and $m\vec{r} \times \ddot{\vec{\theta}}$, known as the Coriolis force and Euler force, respectively. Equation (A8) is well known in the literature and gives rise, among other things, to the Sagnac effect [58–61].

The Lagrangian term $m\dot{\theta}(-x v_y + v_x y)$ can be written in polar coordinates with $x = r\cos\phi$ and $y = r\sin\phi$ [see Fig. 9(a)]. If r is assumed constant, then $v_x = -r\dot{\phi}\sin\phi$ and $v_y = r\dot{\phi}\cos\phi$, so this term becomes $-mr^2\dot{\theta}\dot{\phi}$. In the special case shown in Fig. 9(b) when the test mass is set on the x axis of the inertial (nonrotating) reference frame, one may directly obtain $\phi = -\theta$. Then, the Lagrangian of the Coriolis and Euler forces becomes $m\dot{\theta}^2 r^2$. Therefore, the total Lagrangian of the centrifugal, Coriolis, and Euler forces reduces to

$$L_{\text{ITN}} = \frac{1}{2} m\dot{\theta}^2 r^2. \tag{A9}$$

Finally, if the angle θ is assumed to be small, then the y component is much smaller than the x component in the Lagrangian. Hence, making the approximation $r \approx x$, we finally obtain the ITN Lagrangian in Eq. (5).

APPENDIX B: CALCULATION OF THE POWER SPECTRUM DENSITY OF INERTIAL TORSION NOISE

In this appendix, we calculate the PSD of the ITN arising from a thermal environment modeled by Eq. (C1). As discussed in the main text, the PSD of ITN $S_{\dot{\Theta}^2\dot{\Theta}^2}(\omega)$ is the self-convolution of the PSD of the torsion angle $S_{\dot{\Theta}\dot{\Theta}}(\omega) = \omega^2 S_{\Theta\Theta}(\omega)$, that is,

$$\begin{aligned} S_{\dot{\Theta}^2\dot{\Theta}^2}(\omega) &= (S_{\dot{\Theta}\dot{\Theta}} * S_{\dot{\Theta}\dot{\Theta}})(\omega) \\ &= \int_{-\infty}^{\infty} (2\gamma_{\text{rot}} k_B T/I)^2 \frac{u^2}{(u^2 - \Omega_{\text{rot}}^2)^2 + \gamma_{\text{rot}}^2 u^2} \\ &\quad \times \frac{(\omega - u)^2}{((\omega - u)^2 - \Omega_{\text{rot}}^2)^2 + \gamma_{\text{rot}}^2 (\omega - u)^2} du. \end{aligned} \tag{B1}$$

We use the residue theorem to calculate this integral [62]. First, the poles of $S_{\Theta\Theta}(\omega)$ are

$$\omega_{1,2,3,4} = \pm\sqrt{\Omega_{\text{rot}}^2 - \gamma_{\text{rot}}^2/4} \pm i\gamma_{\text{rot}}/2. \tag{B2}$$

The positiveness of the discriminant $\Omega_{\text{rot}}^2 - \gamma_{\text{rot}}^2/4$ will affect the positions of poles of the integrand in Eq. (B1), shown in Fig. 10, of which the discriminants in Figs. 10(a) and 10(b) are positive and negative, respectively. Note that the relations $\omega_3 = -\omega_2$ and $\omega_4 = -\omega_1$ are used to simplify the notation in both panels. However, since the integral is real valued, both cases should have the same result. Thus, it is enough to consider the case $\Omega_{\text{rot}}^2 - \gamma_{\text{rot}}^2/4 > 0$.

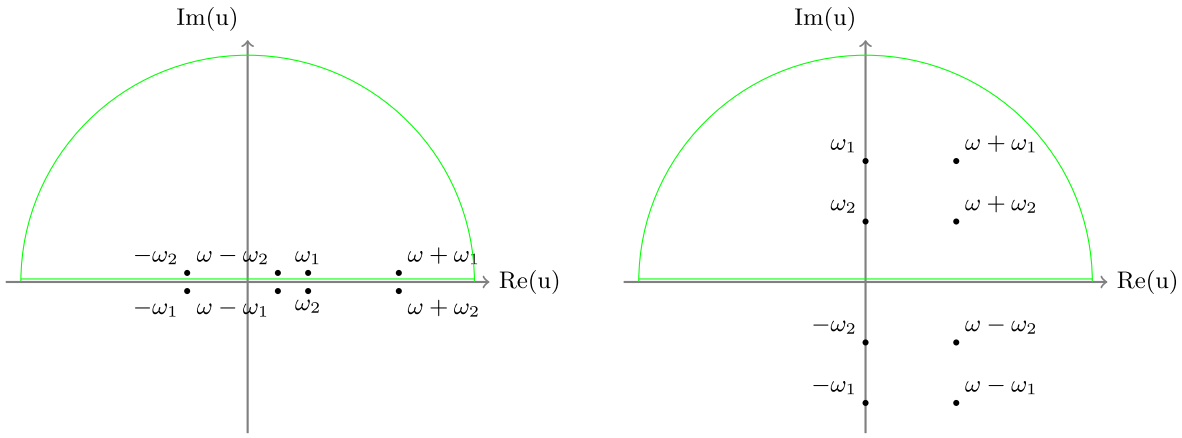

FIG. 10. Poles and integral path of the integral in Eq. (B1). The poles of $S_{\Theta\Theta}$ and $S_{\dot{\Theta}^2\dot{\Theta}^2}(\omega)$ are given by Eq. (B2). Panels (a) and (b) show two cases where $\sqrt{\Omega_{\rm rot}^2-\gamma_{\rm rot}^2/4}$ is a real number and an imaginary number. Note that the relations $\omega_3=-\omega_2$ and $\omega_4=-\omega_1$ are used to simplify the notation in both panels.

Then, according to the residue theorem, the integral value in Eq. (B1) equals the residue value of the integrand at the poles in the path shown in Fig. 10. In particular, this integral equals the summation of the residues at ω_1, $-\omega_2$, $\omega+\omega_1$, and $\omega-\omega_2$ when $\omega\neq\omega_1+\omega_2$. In this case, every pole is a first-order pole. For the special case $\omega=\omega_1+\omega_2$, there are only two second-order poles ω_1 and ω_2, so the integral in Eq. (B1) is given by these two poles. Since our purpose is to calculate the pure real-valued integral (B1) and different cases of poles have to give the same result, we may focus on the case $\omega\neq\omega_1+\omega_2=2\sqrt{\Omega_{\rm rot}^2-\gamma_{\rm rot}^2/4}$. Then, the integrand can be written as

$$F(u,\omega)=A^2\frac{u^2(\omega-u)^2}{(u-\omega_1)(u-\omega_2)(u+\omega_1)(u+\omega_2)}\times\frac{1}{(u-(\omega-\omega_1))(u-(\omega-\omega_2))(u-(\omega+\omega_1))(u-(\omega+\omega_2))},\tag{B3}$$

where we denote $A=2\gamma_{\rm rot}k_BT/I$ for ease of notation. Then, the residue values are given by

$$\begin{aligned}
2\pi{\rm i}\operatorname*{Res}_{u=\omega_1}F(u)&=A^2\frac{\pi\omega_1(\omega-\omega_1)^2}{2\gamma_{\rm rot}\sqrt{\Omega_{\rm rot}^2-\gamma_{\rm rot}^2/4}}\times\frac{1}{\omega(\omega-{\rm i}\gamma_{\rm rot})(\omega-2\sqrt{\Omega_{\rm rot}^2-\gamma_{\rm rot}^2/4})(\omega-2\omega_1)},\\
2\pi{\rm i}\operatorname*{Res}_{u=-\omega_2}F(u)&=A^2\frac{\pi\omega_2(\omega+\omega_2)^2}{2\gamma_{\rm rot}\sqrt{\Omega_{\rm rot}^2-\gamma_{\rm rot}^2/4}}\times\frac{1}{\omega(\omega-{\rm i}\gamma_{\rm rot})(\omega+2\sqrt{\Omega_{\rm rot}^2-\gamma_{\rm rot}^2/4})(\omega+2\omega_2)},\\
2\pi{\rm i}\operatorname*{Res}_{u=\omega+\omega_1}F(u)&=A^2\frac{(\omega+\omega_1)^2\omega_1^2}{\omega(\omega+{\rm i}\gamma_{\rm rot})(\omega+2\omega_1)(\omega+2\sqrt{\Omega_{\rm rot}^2-\gamma_{\rm rot}^2/4})}\times\frac{\pi}{2\omega_1\gamma_{\rm rot}\sqrt{\Omega_{\rm rot}^2-\gamma_{\rm rot}^2/4}},\\
2\pi{\rm i}\operatorname*{Res}_{u=\omega-\omega_2}F(u)&=A^2\frac{(\omega-\omega_2)^2\omega_2^2}{\omega(\omega-2\sqrt{\Omega_{\rm rot}^2-\gamma_{\rm rot}^2/4})(\omega-2\omega_2)(\omega+{\rm i}\gamma_{\rm rot})}\times\frac{\pi}{2\omega_2\gamma_{\rm rot}\sqrt{\Omega_{\rm rot}^2-\gamma_{\rm rot}^2/4}}.
\end{aligned}\tag{B4}$$

Finally, the PSD of ITN defined as the integral (B1) is

$$\begin{aligned}
S_{\dot{\Theta}^2\dot{\Theta}^2}(\omega)&=2\pi{\rm i}\Big(\operatorname*{Res}_{u=\omega_1}F(u)+\operatorname*{Res}_{u=-\omega_2}F(u)+\operatorname*{Res}_{u=\omega+\omega_1}F(u)+\operatorname*{Res}_{u=\omega-\omega_2}F(u)\Big)\\
&=A^2\frac{\pi}{\gamma_{\rm rot}}\frac{4\omega^4+4(\gamma_{\rm rot}^2-3\Omega_{\rm rot}^2)\omega^2+16\Omega_{\rm rot}^4}{(\omega^2+\gamma_{\rm rot}^2)(4\gamma_{\rm rot}^2\omega^2+(\omega^2-4\Omega_{\rm rot}^2)^2)}.
\end{aligned}\tag{B5}$$

APPENDIX C: GAS COLLISION NOISE

In this appendix, we consider a certain source of the ITN, that is, collisions due to the thermal motion of gas molecules. According to the fluctuation-dissipation theorem, the amplitude of the random force due to gas collisions is $\sqrt{A}=\sqrt{2\gamma_{\rm rot}k_BT/I}$, where k_B is the Boltzmann constant and $T=300$ K is the gas temperature outside the experimental box. Then, the dynamical equation (17) of the

torsion motion of the experimental box becomes the Langevin equation [63],

$$\ddot{\Theta} = -\Omega_{\rm rot}^2\Theta - \gamma_{\rm rot}\dot{\Theta} + \sqrt{2\gamma_{\rm rot}k_BT/I}\Theta_{\rm in}. \quad \text{(C1)}$$

In this case, the power spectra for Θ and $\dot{\Theta}^2$ are

$$S_{\Theta\Theta}(\omega) = \frac{2\gamma_{\rm rot}k_BT/I}{(\Omega_{\rm rot}^2-\omega^2)^2+\gamma_{\rm rot}^2\omega^2},$$
$$S_{\dot{\Theta}^2\dot{\Theta}^2}(\omega) = \frac{4\pi\gamma_{\rm rot}(k_BT)^2}{I^2} \times \frac{4\omega^4+4(\gamma_{\rm rot}^2-3\Omega_{\rm rot}^2)\omega^2+16\Omega_{\rm rot}^4}{(\omega^2+\gamma_{\rm rot}^2)(4\gamma_{\rm rot}^2\omega^2+(\omega^2-4\Omega_{\rm rot}^2)^2)}. \quad \text{(C2)}$$

It is notable that $S_{\dot{\Theta}^2\dot{\Theta}^2}(\omega)$ has an additional γ^2 dependence in comparison with the general case in Eq. (20). This difference arises because the amplitude $A = 2\gamma_{\rm rot}k_BT/I$ of the external force for the thermal noise in Eq. (C1) is proportional to the damping rate $\gamma_{\rm rot}$, which does not hold for the general case considered in this appendix.

Note that, in this case, the damping rate $\gamma_{\rm rot}$ describes both the dissipation effect and the random force caused by collisions from the ambient thermal gas molecules, which is given by [64,65]

$$\gamma_{\rm rot} = \frac{L^4}{I}\left(1+\frac{\pi}{12}\right)P_{\rm gas}\sqrt{\frac{2m_{\rm gas}}{\pi k_BT}}, \quad \text{(C3)}$$

where $P_{\rm gas}$ is the pressure of gas and $m_{\rm gas}$ is the mass of the gas molecules. Since $\gamma_{\rm rot}$ is proportional to $P_{\rm gas}$, it can vary depending on the gas pressure outside the box. Apart from $P_{\rm gas}$, all other factors contribute a factor of around 10^{-4}–10^{-3} Hz/Pa, so the value of the damping rate $\gamma_{\rm rot}$ can be estimated as

$$\gamma_{\rm rot}/[\rm Hz] \sim 10^{-4}P_{\rm gas}/[\rm Pa]. \quad \text{(C4)}$$

For instance, in the atmosphere, $P_{\rm gas} = 10^5$ Pa and the damping rate is $\gamma_{\rm rot} \sim 10^1$ Hz. When the gas pressure outside the experimental box is pumped as 10^2 Pa or 10^{-6} Pa by a rough-vacuum pump or a series of ultra-high-vacuum pumps, respectively, the corresponding damping rates $\gamma_{\rm rot}$ are 10^{-2} and 10^{-10} Hz, respectively. Note that a value $\gamma_{\rm rot} \sim 10^{-9}$ Hz was already experimentally measured [64].

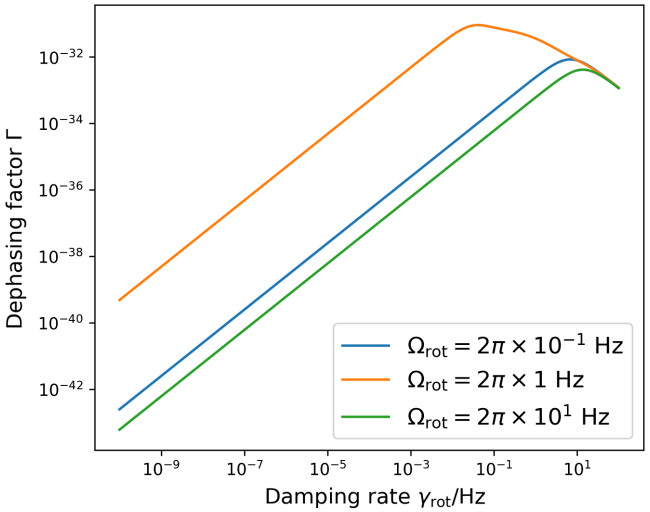

FIG. 11. Dephasing factor Γ as a function of the damping factor $\gamma_{\rm rot}$ for the thermal case. The transfer function is given in Eq. (11) with parameters $t_a = 0.25$ s and $t_e = 0$ s. Three different $\Omega_{\rm rot}$ are chosen in the low rotation frequency limit (blue line), the resonance frequency condition $\Omega_{\rm rot} \sim 2\pi/T = 2\pi$Hz (orange line), and the high rotation frequency limit (green line). The dephasing Γ is proportional to $\gamma_{\rm rot}$ when $\gamma_{\rm rot} \ll \Omega_{\rm rot}$, while it starts decreasing with respect to $\gamma_{\rm rot}$ when $\gamma_{\rm rot}$ becomes comparable to or larger than $\Omega_{\rm rot}$.

As for the dephasing factor, Fig. 11 shows the dependence of Γ on the damping factor $\gamma_{\rm rot}$ caused by the thermal gas molecules. As is shown, for the thermal case, Γ is proportional to $\gamma_{\rm rot}$ and $\gamma_{\rm rot}^{-1}$ in the underdamped region and the overdamped region, respectively, which has an additional γ^2 dependence in comparison with the general case because the thermal amplitude A^2 is proportional to $\gamma_{\rm rot}^2$.

A final remark on Fig. 11 is that the dephasing factor Γ caused by the torsion noise from gas molecule collisions is negligibly tiny. Two main reasons cause this. First, the thermal motion of gas molecules is proportional to a small thermal factor $k_BT \sim 10^{-21}$ J. Besides, ITN is a second-order effect, so every little factor in the PSD $S_{\Theta\Theta}(\omega)$ of the experimental apparatus will be squared for the dephasing factor Γ. Combining both effects, the dephasing factor Γ is suppressed by a very tiny factor $(k_BT)^2 \sim 10^{-42}$ J^2, such that Γ does not exceed 10^{-30}.

[1] Achim Peters, Keng Yeow Chung, and Steven Chu, Measurement of gravitational acceleration by dropping atoms, Nature (London) **400**, 849 (1999).

[2] J. B. Fixler, G. T. Foster, J. M. McGuirk, and M. A. Kasevich, Atom interferometer measurement of the Newtonian constant of gravity, Science **315**, 74 (2007).

[3] Ben Stray *et al.*, Quantum sensing for gravity cartography, Nature (London) **602**, 590 (2022).
[4] Jack C. Saywell *et al.*, Enhancing the sensitivity of atom-interferometric inertial sensors using robust control, Nat. Commun. **14**, 7626 (2023).
[5] Vladimir V. Soshenko, Stepan V. Bolshedvorskii, Olga Rubinas, Vadim N. Sorokin, Andrey N. Smolyaninov, Vadim V. Vorobyov, and Alexey V. Akimov, Nuclear spin gyroscope based on the nitrogen vacancy center in diamond, Phys. Rev. Lett. **126**, 197702 (2021).
[6] Chris Overstreet, Peter Asenbaum, Tim Kovachy, Remy Notermans, Jason M. Hogan, and Mark A. Kasevich, Effective inertial frame in an atom interferometric test of the equivalence principle, Phys. Rev. Lett. **120**, 183604 (2018).
[7] Peter Asenbaum, Chris Overstreet, Minjeong Kim, Joseph Curti, and Mark A. Kasevich, Atom-interferometric test of the equivalence principle at the 10^{-12} level, Phys. Rev. Lett. **125**, 191101 (2020).
[8] Sougato Bose, Anupam Mazumdar, Martine Schut, and Marko Toroš, Entanglement witness for the weak equivalence principle, Entropy **25**, 448 (2023).
[9] Sougato Bose, Anupam Mazumdar, Gavin W. Morley, Hendrik Ulbricht, Marko Toroš, Mauro Paternostro, Andrew A. Geraci, Peter F. Barker, M. S. Kim, and Gerard Milburn, Spin entanglement witness for quantum gravity, Phys. Rev. Lett. **119**, 240401 (2017).
[10] Sougato Bose (QGEM Collaboration), https://www.youtube.com/watch?v=0Fv-0k13s_k (2016) Accessed 1/11/22.
[11] C. Marletto and V. Vedral, Gravitationally induced entanglement between two massive particles is sufficient evidence of quantum effects in gravity, Phys. Rev. Lett. **119**, 240402 (2017).
[12] Ryan J. Marshman, Anupam Mazumdar, and Sougato Bose, Locality and entanglement in table-top testing of the quantum nature of linearized gravity, Phys. Rev. A **101**, 052110 (2020).
[13] Daniel Carney, Newton, entanglement, and the graviton, Phys. Rev. D **105**, 024029 (2022).
[14] Dripto Biswas, Sougato Bose, Anupam Mazumdar, and Marko Toroš, Gravitational optomechanics: Photon-matter entanglement via graviton exchange, Phys. Rev. D **108**, 064023 (2023).
[15] Shafaq Gulzar Elahi and Anupam Mazumdar, Probing massless and massive gravitons via entanglement in a warped extra dimension, Phys. Rev. D **108**, 035018 (2023).
[16] Ulrich K. Beckering Vinckers, Álvaro de la Cruz-Dombriz, and Anupam Mazumdar, Quantum entanglement of masses with nonlocal gravitational interaction, Phys. Rev. D **107**, 124036 (2023).
[17] B. Canuel *et al.*, The matter-wave laser interferometer gravitation antenna (MIGA): New perspectives for fundamental physics and geosciences, E3S Web Conf. **4**, 01004 (2014).
[18] J. Junca *et al.*, Characterizing Earth gravity field fluctuations with the MIGA antenna for future gravitational wave detectors, Phys. Rev. D **99**, 104026 (2019).
[19] Mahiro Abe *et al.*, Matter-wave atomic gradiometer interferometric sensor (MAGIS-100), Quantum Sci. Technol. **6**, 044003 (2021).
[20] Jeremiah Thomas Mitchell, Tim Kovachy, Steve Hahn, Philip Adamson, and Swapan Chattopadhyay, MAGIS-100 environmental characterization and noise analysis, J. Instrum. **17**, P01007 (2022); **17**, E02001 (2022).
[21] Ryan J. Marshman, Anupam Mazumdar, Gavin W. Morley, Peter F. Barker, Steven Hoekstra, and Sougato Bose, Mesoscopic interference for metric and curvature and gravitational wave detection, New J. Phys. **22**, 083012 (2020).
[22] Thomas W. van de Kamp, Ryan J. Marshman, Sougato Bose, and Anupam Mazumdar, Quantum gravity witness via entanglement of masses: Casimir screening, Phys. Rev. A **102**, 062807 (2020).
[23] Martine Schut, Andrew Geraci, Sougato Bose, and Anupam Mazumdar, Micrometer-size spatial superpositions for the QGEM protocol via screening and trapping, Phys. Rev. Res. **6**, 013199 (2024).
[24] Martine Schut, Alexey Grinin, Andrew Dana, Sougato Bose, Andrew Geraci, and Anupam Mazumdar, Relaxation of experimental parameters in a quantum-gravity-induced entanglement of masses protocol using electromagnetic screening, Phys. Rev. Res. **5**, 043170 (2023).
[25] Mark Keil *et al.*, *Stern-Gerlach Interferometry with the Atom Chip* (Springer International Publishing, Cham, 2021), pp. 263–301.
[26] Shimon Machluf, Yonathan Japha, and Ron Folman, Coherent Stern–Gerlach momentum splitting on an atom chip, Nat. Commun. **4**, 2424 (2013).
[27] Yair Margalit *et al.*, Realization of a complete Stern-Gerlach interferometer: Toward a test of quantum gravity, Sci. Adv. **7**, eabg2879 (2021).
[28] C. Wan, M. Scala, G. W. Morley, A. T. M. A. Rahman, H. Ulbricht, J. Bateman, P. F. Barker, S. Bose, and M. S. Kim, Free nano-object Ramsey interferometry for large quantum superpositions, Phys. Rev. Lett. **117**, 143003 (2016).
[29] Julen S. Pedernales, Gavin W. Morley, and Martin B. Plenio, Motional dynamical decoupling for interferometry with macroscopic particles, Phys. Rev. Lett. **125**, 023602 (2020).
[30] Ryan J. Marshman, Anupam Mazumdar, Ron Folman, and Sougato Bose, Constructing nano-object quantum superpositions with a Stern-Gerlach interferometer, Phys. Rev. Res. **4**, 023087 (2022).
[31] Run Zhou, Ryan J. Marshman, Sougato Bose, and Anupam Mazumdar, Catapulting towards massive and large spatial quantum superposition, Phys. Rev. Res. **4**, 043157 (2022).
[32] Run Zhou, Ryan J. Marshman, Sougato Bose, and Anupam Mazumdar, Mass-independent scheme for enhancing spatial quantum superpositions, Phys. Rev. A **107**, 032212 (2023).
[33] André Großardt, Acceleration noise constraints on gravity-induced entanglement, Phys. Rev. A **102**, 040202 (2020).
[34] Marko Toroš, Thomas W. van de Kamp, Ryan J. Marshman, M. S. Kim, Anupam Mazumdar, and Sougato Bose, Relative acceleration noise mitigation for nanocrystal matter-wave interferometry: Applications to entangling masses via quantum gravity, Phys. Rev. Res. **3**, 023178 (2021).
[35] Meng-Zhi Wu, Marko Toroš, Sougato Bose, and Anupam Mazumdar, Quantum gravitational sensor for space debris, Phys. Rev. D **107**, 104053 (2023).

[36] Paolo Fragolino, Martine Schut, Marko Toroš, Sougato Bose, and Anupam Mazumdar, Decoherence of a matter-wave interferometer due to dipole-dipole interactions, Phys. Rev. A **109**, 033301 (2024).
[37] Martine Schut, Herre Bosma, MengZhi Wu, Marko Toroš, Sougato Bose, and Anupam Mazumdar, Dephasing due to electromagnetic interactions in spatial qubits, Phys. Rev. A **110**, 022412 (2024).
[38] Marko Toroš, Anupam Mazumdar, and Sougato Bose, Loss of coherence and coherence protection from a graviton bath, Phys. Rev. D **109**, 084050 (2024).
[39] Gregory M Harry (LIGO Scientific Collaboration), Advanced LIGO: The next generation of gravitational wave detectors, Classical Quantum Gravity **27**, 084006 (2010).
[40] G. Losurdo *et al.*, An inverted pendulum preisolator stage for the Virgo suspension system, Rev. Sci. Instrum. **70**, 2507 (1999).
[41] Peter R. Saulson, Robin T. Stebbins, Frank D. Dumont, and Scott E. Mock, The inverted pendulum as a probe of an elasticity, Rev. Sci. Instrum. **65**, 182 (1994).
[42] Jean-Charles Dumas, Li Ju, and David G. Blair, Modelling of tuning of an ultra low frequency Roberts linkage vibration isolator, Phys. Lett. A **374**, 3705 (2010).
[43] M. Scala, M. S. Kim, G. W. Morley, P. F. Barker, and S. Bose, Matter-wave interferometry of a levitated thermal nano-oscillator induced and probed by a spin, Phys. Rev. Lett. **111**, 180403 (2013).
[44] Fernando C. Lombardo and Paula I. Villar, Dephasing in matter-wave interferometry, J. Phys. A **39**, 6509 (2006).
[45] Zhang-qi Yin, Tongcang Li, Xiang Zhang, and L. M. Duan, Large quantum superpositions of a levitated nanodiamond through spin-optomechanical coupling, Phys. Rev. A **88**, 033614 (2013).
[46] Xing-Yan Chen and Zhang-Qi Yin, High-precision gravimeter based on a nano-mechanical resonator hybrid with an electron spin, Opt. Express **26**, 31577 (2018).
[47] Ryszard Horodecki, Paweł Horodecki, Michał Horodecki, and Karol Horodecki, Quantum entanglement, Rev. Mod. Phys. **81**, 865 (2009).
[48] Martine Schut, Jules Tilly, Ryan J. Marshman, Sougato Bose, and Anupam Mazumdar, Improving resilience of quantum-gravity-induced entanglement of masses to decoherence using three superpositions, Phys. Rev. A **105**, 032411 (2022).
[49] Jules Tilly, Ryan J. Marshman, Anupam Mazumdar, and Sougato Bose, Qudits for witnessing quantum-gravity-induced entanglement of masses under decoherence, Phys. Rev. A **104**, 052416 (2021).
[50] Thomas W. van de Kamp, Ryan J. Marshman, Sougato Bose, and Anupam Mazumdar, Quantum gravity witness via entanglement of masses: Casimir screening, Phys. Rev. A **102**, 062807 (2020).
[51] Pippa Storey and Claude Cohen-Tannoudji, The Feynman path integral approach to atomic interferometry: A tutorial, J. Phys. II (France) **4**, 1999 (1994).
[52] Meng-Zhi Wu, Acceleration noise induced decoherence in Stern-Gerlach interferometers for gravity experiments, arXiv:2406.10832.
[53] P. Mohazzabi and B. M. Shefchik, A universal relationship between spring constant and torsion constant, J. Phys. Chem. Solids **62**, 677 (2001).
[54] Stephen H. Crandall, Norman C. Dahl, and Ellis Harold Dill, An Introduction to the Mechanics of Solids (McGraw-Hill, Boston, 1959).
[55] Quentin Beaufils, Julien Lefebve, Joel Gomes Baptista, Raphaël Piccon, Valentin Cambier, Leonid A. Sidorenkov, Christine Fallet, Thomas Lévèque, Sébastien Merlet, and Franck Pereira Dos Santos, Rotation related systematic effects in a cold atom interferometer onboard a nadir pointing satellite, NPJ Microgravity **9**, 53 (2023).
[56] Eric Poisson, Adam Pound, and Ian Vega, The motion of point particles in curved spacetime, Living Rev. Relativity **14**, 7 (2011).
[57] Weihuan Chen, Shiing-shen Chern, and Kai S. Lam, *Lectures on Differential Geometry* (World Scientific Publishing Company, Singapore, 1999), Vol. 1.
[58] Evert Jan Post, Sagnac effect, Rev. Mod. Phys. **39**, 475 (1967).
[59] Ronald Anderson, H. R. Bilger, and G. E. Stedman, Sagnac effect: A century of Earth-rotated interferometers, Am. J. Phys. **62**, 975 (1994).
[60] Grigorii B. Malykin, The Sagnac effect: Correct and incorrect explanations, Phys. Usp. **43**, 1229 (2000).
[61] Marko Toroš, Sara Restuccia, Graham M. Gibson, Marion Cromb, Hendrik Ulbricht, Miles Padgett, and Daniele Faccio, Revealing and concealing entanglement with non-inertial motion, Phys. Rev. A **101**, 043837 (2020).
[62] George B. Arfken, Hans-Jurgen Weber, and Frank E. Harris, *Mathematical Methods for Physicists: A Comprehensive Guide* (Academic Press, 2011).
[63] Don S. Lemons and Anthony Gythiel, Sur la thiorie du mouvement brownien, C. R. Acad. Sci. (Paris) **146**, 530 (1908) [Paul Langevin's 1908 paper on the theory of Brownian motion, Am. J. Phys. **65**, 1079 (1997)].
[64] A. Cavalleri, G. Ciani, R. Dolesi, A. Heptonstall, M. Hueller, D. Nicolodi, S. Rowan, D. Tombolato, S. Vitale, P. J. Wass, and W. J. Weber, Increased Brownian force noise from molecular impacts in a constrained volume, Phys. Rev. Lett. **103**, 140601 (2009).
[65] A. Cavalleri, G. Ciani, R. Dolesi, M. Hueller, D. Nicolodi, D. Tombolato, S. Vitale, P. J. Wass, and W. J. Weber, Gas damping force noise on a macroscopic test body in an infinite gas reservoir, Phys. Lett. A **374**, 3365 (2010).